The Relationship between Structural and Electrical Characteristics in Perylenecarboxydiimide-Based Nanoarchitectures

*Chiara Musumeci, Ingo Salzmann, Sara Bonacchi, Christian Röthel, Steffen Duhm, Norbert Koch, and Paolo Samorì**

The controlled assembly of the prototypical n-type organic semiconductor N,N′-1H,1H-perfluorobutyl dicyanoperylenecarboxydiimide (PDIF-CN_2) into ordered nanoarchitectures and the multiscale analysis of the correlation between their structural and their electrical properties is reported. By making use of the Langmuir–Blodgett (LB) technique, monolayers of PDIF-CN_2 arranged in upright standing molecular packing on different substrates are formed. Postdeposition thermal treatment makes it possible to trigger a reorganization into layered ultrathin crystalline nanostructures, exhibiting structural and photophysical properties similar to those of microscopic crystals obtained by solvent-induced precipitation. The controlled engineering of these molecular architectures on surfaces enables us to identify both a dependence of the monolayer resistance on the molecular tilt angle in vertical junctions and a pronounced charge-transport anisotropy with enhanced transport along the π–π stacking direction of the PDI core. While a charge carrier mobility for electrons as high as 10^{-2} cm^2 V^{-1} s^{-1} is determined in monolayer field-effect transistors for the in-plane direction, being the highest yet reported value for a n-type LB monolayer, the out-of-plane mobility measured by conductive atomic force microscopy in multilayered structures is found to be one order of magnitude lower.

1. Introduction

Downscaling organic thin-film transistors by reducing the thickness of the functional semiconductor layer,[1] that of the dielectric layer,[2] or by reducing the size of the inter-electrode gap (i.e., the source –drain distance) in organic field-effect transistors (OFETs) is among the greatest challenges in organic (nano)electronics.[3] Shrinking the dimension of the individual components can, in fact, lead to a marked improvement of the device performance. In particular, the possibility of using only few nanometer thick active layers exhibiting high charge mobility in a bottom contact/bottom gate configuration is highly relevant for sensing applications. In the latter, changes of the electrical characteristics of the OFET are expected due to physical/chemical interaction between the semiconductor and the analyte.[4] In this context, multiscale investigations of the conduction properties of electroactive organic materials assembled in low-dimensional nanostructures is expected to improve the fundamental understanding of the charge transport mechanisms reflecting the bulk electrical behavior.

Here, we report a multiscale study on the correlation between structural and electrical characteristics in highly ordered nanoscale architectures employing a well-known perylene diimide (PDI) derivative. This materials class has yet been widely used in organic electronics as n-type semiconductor in OFETs[5] and as electron acceptor in organic solar cells,[6] as it combines relatively high electron affinity and mobility with excellent chemical, thermal, and photochemical stability.[7] In particular, N,N′-1H,1H-perfluorobutyl dicyanoperylenecarboxydiimide (PDIF-CN_2, **Figure 1**a) has been thoroughly investigated because of its excellent stability in air and its promising transport properties for electrons.[8]

Single crystals of PDIF-CN_2 exhibit a crystal structure characterized by a slightly twisted polycyclic core with slip-stacked face-to-face molecular packing and an inter-plane spacing of 3.40 Å.[8] This motif, enabling significant intermolecular π–π overlap, is considered responsible for the excellent charge transport properties.[8] The highest mobility

Dr. C. Musumeci,[+] Dr. S. Bonacchi, Prof. P. Samorì
ISIS and icFRC, Université de Strasbourg and CNRS
8 allée Gaspard Monge
67000 Strasbourg, France
E-mail: samori@unistra.fr
Dr. I. Salzmann, Prof. N. Koch
Institut für Physik and IRIS Adlershof
Humboldt-Universität zu Berlin, Brook-Taylor-Straße 6
12489 Berlin, Germany
C. Röthel
Institut für Festkörperphysik
Graz University of Technology
Petersgasse 16
8010 Graz, Austria
Prof. S. Duhm, Prof. N. Koch
Institute of Functional Nano and Soft Materials (FUNSOM)
Soochow University
Suzhou 215123, China
[+]Present address: Biomolecular and organic electronics, Dept. of Physics, Chemistry, and Biology IFM, Linköping University, 58183 Linköping, Sweden.

DOI: 10.1002/adfm.201403773

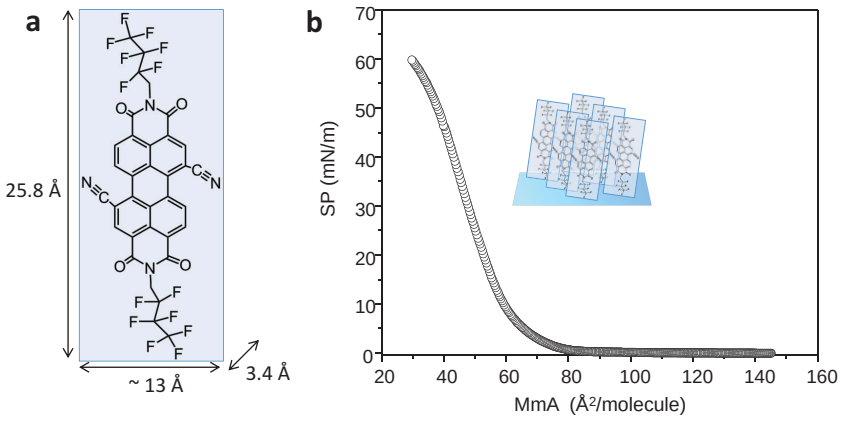

Figure 1. a) Molecular structure of PDIF-CN_2. b) Surface pressure versus mean molecular area curve for the film formation at the air–water interface obtained by the Langmuir–Blodgett technique. The scheme in the inset shows the suggested molecular arrangement in the condensed phase.

reported for single crystals of this molecule is, indeed, in the range of 1–6 $cm^2\ V^{-1}\ s^{-1}$.[9] Large crystals hundreds of nanometers wide, grown from solution have also shown a mobility of 1.3 $cm^2\ V^{-1}\ s^{-1}$.[10] PDIF-CN_2-based OFETs, where the semiconductor is thermally sublimed forming polycrystalline films, exhibit a mobility of 0.7 $cm^2\ V^{-1}\ s^{-1}$,[11] while 0.15 $cm^2\ V^{-1}\ s^{-1}$ is measured in vacuum in a bottom-gate/bottom-contact transistor configuration after thermal treatment of the spin-coated polycrystalline films.[12] The edge-on orientation of the PDIF-CN_2 molecules with respect to the substrate plane was demonstrated to enhance the OFET performance after this treatment.[12,13]

Langmuir-based techniques are among the most promising methods to produce ordered monomolecular thin films; they have been employed with great success to control the assembly of both conjugated polymers[14] and small molecules[15] for organic electronic devices,[16] and to form model systems for fundamental studies on the charge transport behavior.[1c,17] Within this work, we make use of this method to fabricate nanoscale-controlled architectures of PDIF-CN_2. In particular, we employ the Langmuir–Blodgett (LB) technique to assemble monomolecular layers with alterable molecular tilt angle and exploit postdeposition thermal treatment in order to promote structural reorganization, finally, generating nanoscopic crystalline architectures. Their electrical characteristics were explored at the nanoscale when integrated in conductive atomic force microscopy (C-AFM)-based junctions, as well as at the microscale in OFET devices.

2. Results and Discussion

2.1. Langmuir–Blodgett Monolayer

2.1.1. Assembly at the Air Water-Interface

Figure 1 displays the surface pressure (SP) versus mean molecular area (Mma) curve as obtained for PDIF-CN_2 molecules spread on the water sub-phase from chloroform solution by compressing with two mobile barriers. The curve exhibits a clear transition from an expanded to a condensed phase.[18] By considering a molecular length of 25.8 Å (including the van der Waals radii of the terminating fluorine atoms),[8,19] an estimated width of ca. 13 Å (ChemDraw) and a π–π spacing of 3.4 Å in the single-crystal structure,[8] a face-on conformation of the molecules in the condensed phase can be clearly ruled out. Instead, the limiting area at zero pressure (around 63 $Å^2$) would correspond to a conformation, where the molecules pack in an edge-on configuration with their long axes tilted with respect to the water surface. The SP versus Mma curves are not steep but they rather rise gradually suggesting that the molecules further tilt upon compression, moving toward a fully standing configuration at higher pressure.[18,20] It is noteworthy, indeed, that the area at which the film starts to collapse (around SP = 52×10^{-3} N m^{-1}) is slightly below 40 $Å^2$, indicating that the molecules, before collapsing, are standing on the water with their long axis almost perpendicular to the surface.

2.1.2. LB Monolayer on Solid Substrates

The transfer of monolayers from the air/water interface onto solid substrates was performed at SPs of 20×10^{-3} N m^{-1} and 45×10^{-3} N m^{-1} by an upstroke operation; the area per molecule at the transfer pressure was 56 and 43 $Å^2$, respectively. The films were successfully transferred onto different substrates, such as gold (Figure 3a), SiO_2, and glass (see Figure S2, Supporting Information). In all cases, the final morphologies that were obtained appeared very similar: they resembled that of typical LB monolayer films consisting of islands aggregated upon compression at the air–water interface. The estimated coverage exceeded 80%. The film thickness was ca. 1.5 nm for the films transferred at 20×10^{-3} N m^{-1}, and ca. 2 nm for the films transferred at 45×10^{-3} N m^{-1}, as inferred from topographical profiles in AFM images. This observation supports a picture in which the molecules within the film have a lower tilt angle with respect to the surface plane when transferred at lower pressure, hence a smaller thickness is measured. When higher pressure is applied, the molecules are almost fully standing on the surface as evidenced by a layer thickness that is similar to the length of the molecule.

To assess the structure of the monolayer, we performed X-ray reflectivity (XRR) of the film deposited at 45×10^{-3} N m^{-1} on SiO_2. **Figure 2**a shows the experimental data together with a fit employing the Parratt[21] formalism based upon a three-layer model for the organic adsorbate, as illustrated in the inset. Recent XRR data for a self-assembled monolayer of a similar, but only one-end fluorinated PDI-derivative allowed determining the thickness of the perfluorobutyl region to 6.0 Å.[22] By assuming, in analogy, two layers of 6.0 Å above and below the PDI backbone, we find 24.9 Å for the overall thickness of our PDIF-CN_2 monolayer

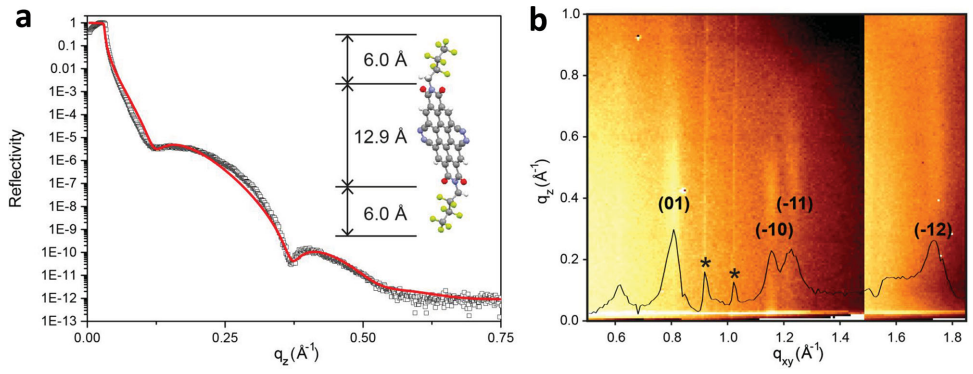

Figure 2. a) XRR data and best fit (red curve) employing a three-layer model (inset) for the PDIF-CN_2 monolayer on SiO_2. b) GIXRD reciprocal space map showing diffracted intensity as a function of the components of the scattering vector (q_{xy}, q_z); the black curve represents the diffraction intensity as integrated along q_z for the area shown in the map; stars mark experimental artefacts due to the separated panels of the Pilatus (DECTRIS) detector. The Bragg rods labeled with the respective Miller indices (*h k*) are indicative of 2D crystalline in-plane order of the monolayer; they allow determining the surface unit cell and estimating the backbone tilt angle (see text).

by fitting the XRR data, which is only slightly less than the molecular length indicating an (almost) upright standing orientation. Since XRR does not allow drawing conclusions on the crystallinity of the layer, we performed grazing-incidence X-ray diffraction (GIXRD) on the film. The corresponding reciprocal space map is shown in Figure 2b. Clearly, four Bragg rods are observed, which indicates that the LB monolayer exhibits in-plane crystalline order. The rods are assigned to (01), (–10), (–11), and (–12) in accordance with the strongest reflections of the PDIF-CN_2 single-crystal structure.[8] From the respective in-plane components of the scattering vector (q_{xy}) the surface-unit cell can be refined to $a = 5.61 \pm 0.01$ Å, $b = 8.05 \pm 0.01$ Å, and $\gamma = 104.75 \pm 0.15°$; note that this value of γ equals that of the reported single-crystal structure, while both *a* and *b* are slightly enlarged by ca. 7%. Importantly, the rods observed in GIXRD are not uniform, as would be expected for a monolayer formed by fully upright standing, rod-like molecules,[1a,23] but show enhanced intensities at values of, e.g., $q_z = 0.4$ Å^{-1} [(10) rod] or at $q_z = 0.6$ Å^{-1} [(–12) rod]. Assuming a similarly π-stacked packing motif as in the single-crystal structure, the structure factor is expected to be particularly high perpendicular to the backbone plane [e.g., (–122) of the single crystal structure]. From the *q*-coordinates of the respective intensity maxima, therefore, the inclination of the molecular backbone with respect to the substrate normal can be estimated to ArcTan(q_{xy}/q_z) ≈ 20°. This value is similar to half of the angle that the perfluorobutyl chains are tilted off the PDI backbone plane (44.8°), hence, corroborating the notion of (almost) fully upright-standing molecular packing in the PDIF-CN_2 monolayer.

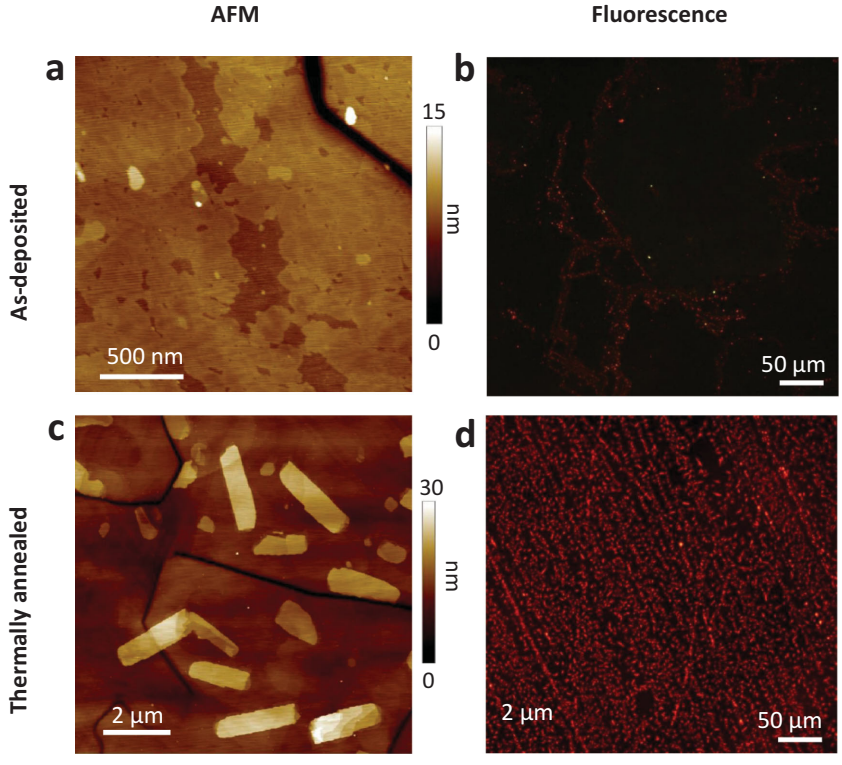

Figure 3. a,c) Representative AFM and b, d) fluorescence microscopy images of the LB monolayer transferred at SP of 45×10^{-3} N m^{-1}: a,b) as deposited and c,d) after thermal annealing. The substrate is gold for (a,c) and glass for (b,d).

2.2. Effect of the Thermal Annealing

Thermal annealing of both LB monolayer films (transferred at SPs of 20×10^{-3} N m^{-1} and 45×10^{-3} N m^{-1}) lead to a notable change in the film morphology, ultimately exhibiting elongated ultrathin nanocrystals featuring well defined, layered structures (**Figures 3**c and S4,S5, Supporting Information) and a characteristic photoluminescence emission in the red region of the spectrum (Figure 3d). The steps in height amount to ca. 2 nm, suggesting that the molecules adopt an almost upright orientation.

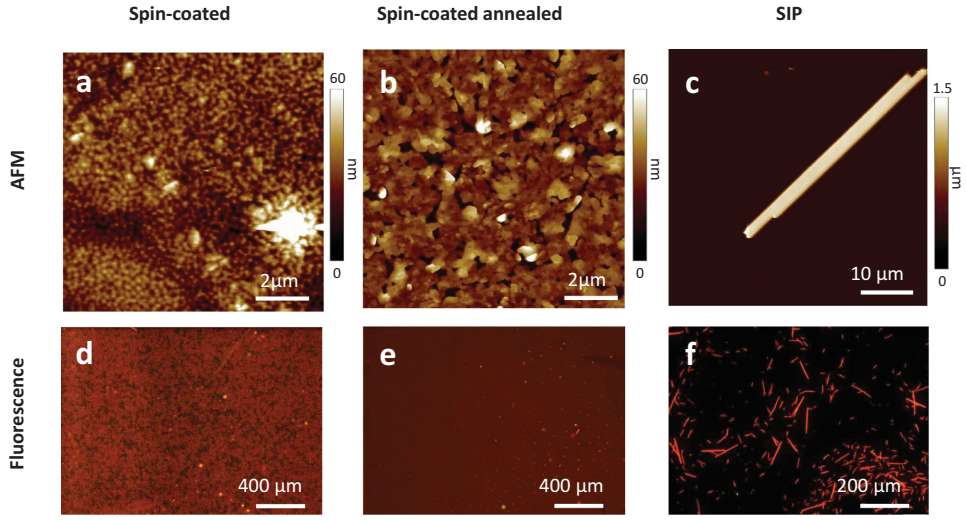

Figure 4. AFM micrographs (top) and fluorescence microscopy images (bottom) of different films on glass substrates: a,d) spin-coated, b,e) spin-coated after thermal annealing, and c,f) drop cast of fibers obtained by SIP.

Note that such a reorganization and final morphology are similar to that reported for thermally annealed spin-coated PDIF-CN_2 films[13] as well as to thermally evaporated films.[24]

To gain insight into the molecular packing, we carried out spectroscopic and morphological analyses on the as-deposited and thermally annealed LB films. We compared these data to that of thin films prepared by spin-coating (SC) and films comprising microscopic fibers produced by solvent-induced precipitation (SIP) and drop cast on glass substrates; the AFM and fluorescence images are shown in **Figure 4**. The AFM micrograph of the SC film (Figure 4a) shows a morphology consisting of small grains [ca. 100 nm in diameter, root mean-square roughness (R_{RMS}) of 6.2 nm in a 5 × 5 µm^2 area]. As expected,[12,13,25] we observe a molecular rearrangement within these films upon thermal annealing (Figure 4b), as evidenced by the appearance of layered, interconnected features (R_{RMS} = 8.2 nm in 5 × 5 µm^2; cf. Figure S6, Supporting Information). Upon SIP, both AFM (Figure 4c) and fluorescence microscopy (Figure 4f) evidenced the rearrangement of the PDIF-CN_2 molecules from homogenously emitting films (Figure 4d,e) to single fluorescent fibers (Figure 4f); the layered nature of the SIP structures has been discussed elsewhere.[26]

The differences in the photophysical properties of these films are shown in **Figure 5**. Compared with the spectrum of PDIF-CN_2 in chloroform solution, the absorption maximum for the LB film is red-shifted from 523 to 560 nm, and the emission spectrum shows negligible Stokes shift (Figure 5a). These data indicate a "head-to-tail" (J-aggregate) orientation of the PDIF-CN_2 in the LB film (transferred at SP 45 × 10^{-3} N m^{-1}). Vice-versa, the spin-coated film exhibits absorption spectra characteristic of perylene chromophores aligned face-to-face (H-aggregate); this H-like aggregation is responsible for the broadening and blue-shift of the absorption spectra of PDIF-CN_2 in the SC film. The oscillator strength of the higher energy transition (≈485 nm) is, indeed, enhanced relative to the lowest energy band (≈520 nm).[27] Interestingly, however, after thermal annealing, the LB film likewise exhibits a substantially blue-shifted and broadened absorption spectrum (Figure 5b) and its photophysical properties are similar to those of the SC film after identical treatment. Moreover, both films show a strong, red-shifted emission maximum in photoluminescence, as compared with that of the film before annealing. In-line with the AFM results, these data indicate pronounced structural reorganization of PDIF-CN_2 in the LB film induced by the thermal treatment; in particular, the red-shifted emission spectra of the

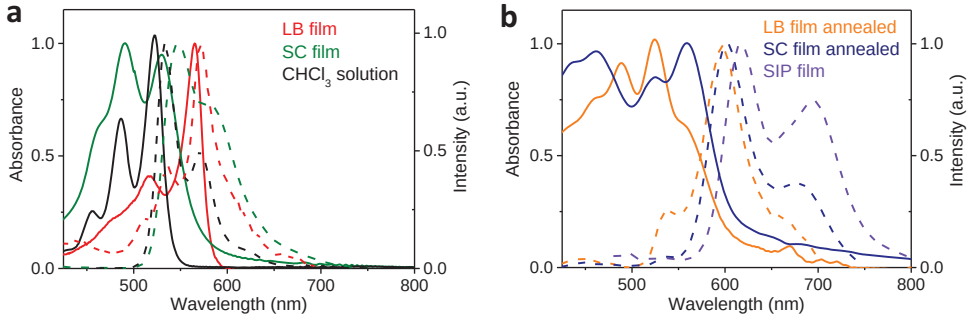

Figure 5. a) Normalized absorption (solid line) and fluorescence spectra (dashed line, λ_{exc} = 395 nm) of PDIF-CN_2 in $CHCl_3$ (black), of the LB (red), and of the SC film (green). b) LB (orange) and SC (blue) films after thermal annealing, and the fibers from SIP (purple).

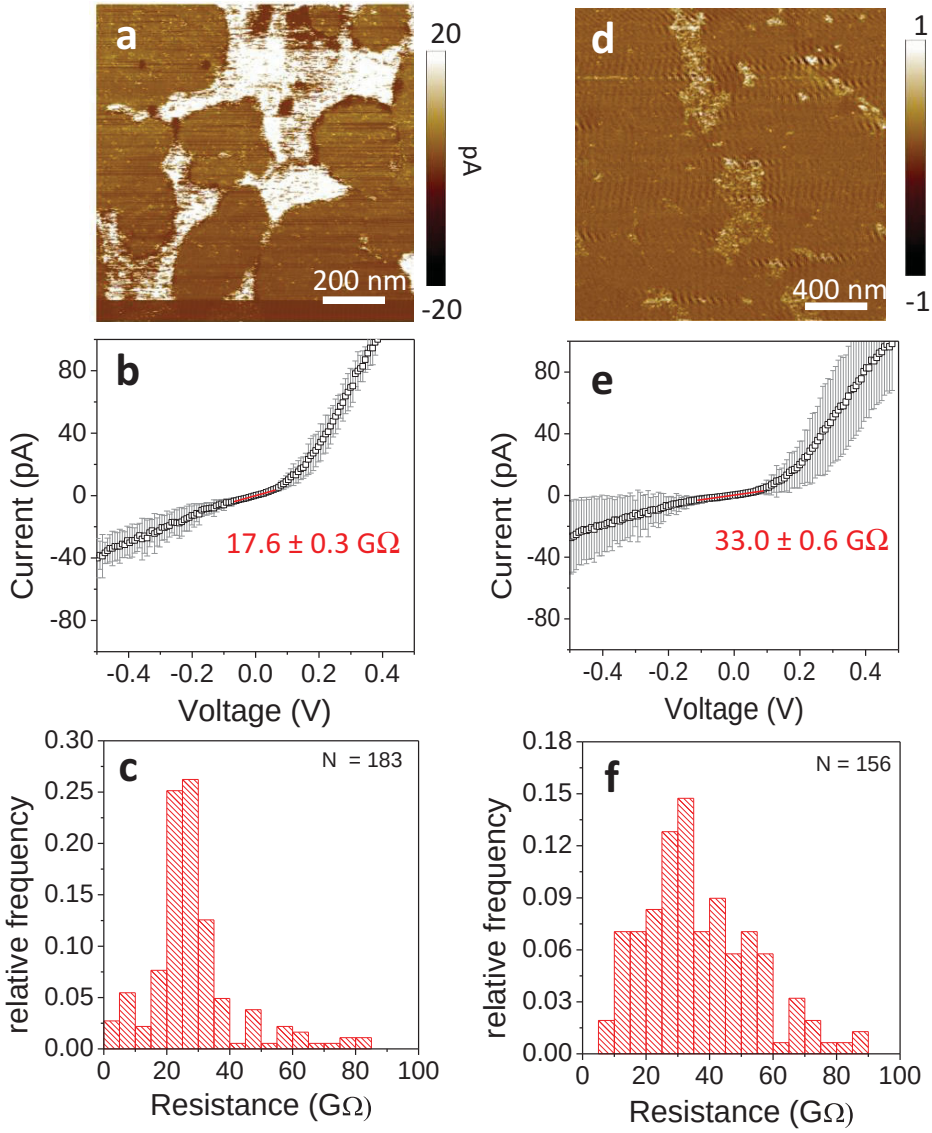

Figure 6. Electrical characterization performed by C-AFM of the monolayer deposited on gold at SP of a–c) 20×10^{-3} N m^{-1}, and d–f) 45×10^{-3} N m^{-1}. a) Current map at 100 mV bias. d) Current map at 10 mV bias. b,e) Average *I–V* curves based on 183 and 156 working junctions, respectively; the grey areas represent the standard error of the average. c,f) Histograms of the resistance values measured from the slope of the single *I–V* curves in the low bias range (marked in red in Figure b,e).

films clearly point toward a higher degree of cofacial arrangement of the molecules in the films.[25] This trend reaches its maximum in the film of SIP-induced fibers exhibiting the strongest red-shifted emission spectra (Figure 5b, dashed purple line), which agrees with the interpretation of a larger π–π overlap between neighboring PDIF-CN_2 molecules after thermal treatment. A schematic drawing of the expected orientation of the molecules for the different films is shown in the Scheme S1 (Supporting Information).

2.3. Electrical Characterization of the LB Monolayer in Vertical C-AFM Junctions

The electrical characterization by C-AFM of the monolayers deposited on gold at SPs of 20 and 45×10^{-3} N m^{-1} is shown in **Figure 6**a–f. The micrograph in Figure 6a,d depict the current maps recorded by biasing the gold electrode at 100 and 10 mV, respectively relative to the conductive Pt/Ir tip. The white areas correspond to a saturated current signal from the bare gold substrate, brown areas correspond to current attenuated by the adsorbate, and the dark brown regions represent areas where no current is detected. The curves shown in Figure 6b,e correspond to the average current–voltage characteristics obtained from 170 local measurements on different points of the two films; both the zero-current and the saturated plots originating either from false contacts or direct contact of tip and gold substrate were discarded while ca. 60% (SP: 20×10^{-3} N m^{-1}) and 80% (SP: 45×10^{-3} N m^{-1}) could be used for analysis. The histograms (c, f) show the distribution of the resistance values calculated from the slopes of the individual *I–V* curves in the low

bias region (–100 to 100 mV). The average resistances were estimated 17.6 ± 0.3 GΩ and 33.0 ± 0.6 GΩ for the films prepared at SP of 20 and 45 × 10^{-3} N m^{-1}, respectively. These values are at least one order of magnitude higher than those typically measured for monolayers of conjugated molecules that are chemically linked to metal substrates.[28] The higher resistance of the film deposited at higher surface pressure further corroborates our proposition of an increased tilt angle induced by the barrier compression at the air–water interface.

The *I–V* curves are clearly asymmetric, which points toward favored electron injection from the AFM tip (positively biased Au substrate); the rectification ratio, defined as (current at 0.4 V)/(current at –0.4 V), is about 4. Rectification could be expected if the molecule is placed asymmetrically within a metal/molecule/metal sandwich configuration, for example, because of the presence of one long alkyl chain.[29] In the present case, however, the molecule is structurally symmetric and the frontier molecular orbitals extend over the whole perylene core.[30] The PDIF-CN_2 electron affinity (≈4.5 eV)[5] is in the range of the work function of both Au (≈4.8 – 5.0 eV) and Pt/Ir (≈5.0–5.2 eV).[31] The asymmetry could be a consequence of slightly better energy level matching of the molecular affinity level with the Fermi-level of Pt/Ir. However, in detail, the energy barrier is known to be sensitive to the particular structure and chemical nature of the metal/organic interface and to interfacial dipole formation.[32] Similarly to previous observations[33] on a monolayer of a pentathiophene derivative on a SiO_2/Si^{p+} substrate probed with a Pt C-AFM tip, we could expect the asymmetry to be attributed to different extent of electrode Fermi-level pinning, as it is corroborated by observations on similar PDI molecules on macroscopic junctions.[34] However, enhanced carrier injection from the AFM probe was also ascribed to the high field associated with the probe point contact, resulting from geometrical effects.[35]

2.4. In-Plane Electrical Characterization of the LB Monolayer

To investigate the in-plane electrical properties of the LB monolayer, we focused on the film deposited at 45 × 10^{-3} N m^{-1}, since we expect the monolayer to be less defective at higher SP.

Figure 7 shows the morphology of this monolayer on a SiO_2/Si^{n++} substrate with prepatterned gold electrodes. The film is characterized by directional fractures probably due to instabilities during the transfer process. The corresponding C-AFM current map obtained by varying the bias on the gold electrode of a few Volts shows that the current signal is close to saturation in the regions directly in contact with the electrode, while it drops abruptly at the right edge of the first fracture/boundary. However, the current is detected up to several micrometers apart from the electrode and increases with bias voltage. This indicates that efficient percolation paths for charges are, indeed, present throughout the film in the channel region despite the high contact resistance, as deduced from C-AFM measurements in horizontal configuration (see Figure S7, Supporting Information).

To measure the in-plane charge carrier mobility of the monolayer, we fabricated OFETs devices in bottom-gate/bottom-contact configuration with different channel lengths and we electrically characterized them in controlled atmosphere. The devices bearing shorter channel lengths (L = 2.5–20 µm) featured clear deviations from linearity in the output curves at low bias and the field-effect mobility decreased with decreasing channel length spanning ca. one order of magnitude, which is typical for contact limited devices (Figure S8, Supporting Information).[36] Furthermore, we observed a dependence of the performance on the transfer direction of the film with respect to the electrode orientation. In particular, since the defects of the films are more pronounced in one specific direction as they are due to instabilities during the film transfer from the air/water interface, we expect the percolation paths for charges between source and drain to be affected by the orientation of these defects within the channel. Indeed, the highest performance in terms of mobility was obtained when source and drain electrodes edges were parallel to the transfer direction.

The devices with longer channel lengths (L = 60–120 µm) showed output curves with Ohmic behavior at low bias. The output and transfer characteristics of a representative device with L = 60 µm is shown in **Figure 8**; the average mobility in these devices was (1.5 ± 0.7)10^{-2} cm^2 V^{-1} s^{-1}. The best performing device with L = 60 µm exhibited a saturated mobility of 3.1 × 10^{-2} cm^2 V^{-1} $s^{-1}$and an I_{on}/I_{off} ratio of 10^4.

Overall, the mobility values obtained for the present monolayer devices are indeed, remarkable. A mobility on the order of 10^{-3} cm^2 V^{-1} s^{-1} was previously obtained on self-assembled PDI monolayer field-effect transistors (SAMFETs).[22,37] Although mobility values in the order of 10^{-2} cm^2 V^{-1} s^{-1} were obtained for three layers of the n-type organic semiconductor poly((N,N′-bis(2-octyldodecyl)-naphthalene-1,4,5,8-bis(dicarboximide)-2,6-diyl)-alt-5,5′-(2,2′-bithiophene)) [P(NDI2OD-T2)] in a top-gate FET architecture, the monolayer of the same polymer showed only a one order of magnitude lower saturated mobility.[1c,17] To the best of our knowledge, comparable values were found only for monomolecular layers in *p*-channel FETs[1a,38] It is noteworthy that in these studies, the authors remarked that in the case of not fully covered SAMFETs, long channel transistors >7.5 µm did not show any drain current, because of the absence of percolation paths connecting the monolayer islands in the channel,[1e] while, in contrast, our present PDIF-CN_2 monolayer devices show excellent performance up to channels as long as 120 µm. In long channel devices, as contact resistance can be neglected, the mobility turned out to be almost independent on the channel length (Figure S8, Supporting Information). The slight decrease in mobility from

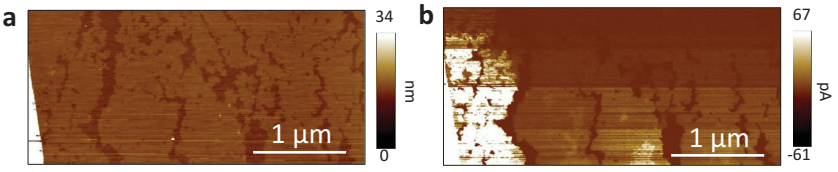

Figure 7. Representative AFM a) topography image and b) current map for a monolayer film deposited on a silicon oxide substrate with prepatterned gold electrode (see the white triangle area on the bottom left corner). The current map is obtained by increasing the bias on the lateral electrode from the top to the bottom of the image scan.

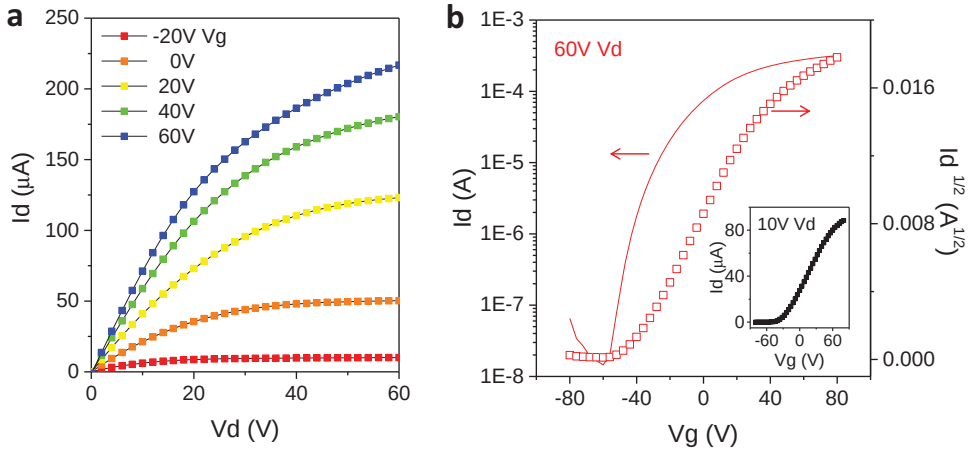

Figure 8. a) Output and b) transfer characteristics of a representative device of 60 μm channel length.

60 to 120 μm of channel length is attributed to the fact that in long channels, the impact of film defects becomes more important in affecting charge transport.[13]

2.5. Out-of-Plane Electrical Characterization of the Layered Nanoscopic Crystals

As shown above, upon thermal annealing, the LB monolayers rearrange to form nanostructures that consist of 1.8–2.0 nm high layers (see Figures 3 and S4,S5, Supporting Information). These structures have been demonstrated to exhibit photophysical, hence structural, properties comparable with those of thermally annealed spin-coated films and microcrystals obtained by SIP. In the following, their vertical charge transport is investigated at the nanoscale by C-AFM using gold substrates as support.

By comparing the average current–voltage characteristics of the LB monolayer as-deposited and one-layer thick planes (1 ML) of the thin nanocrystals obtained after annealing, a reduction of the resistance in the low bias range from 33.0 ± 0.6 GΩ for the untreated LB film transferred at 45 × 10^{-3} N m^{-1} to 22.6 ± 0.4 GΩ for the annealed 1 ML layer (Figure S9, Supporting Information) was observed, as a result of the molecular reorganization. An interesting feature of the *I–V* curve is that in the annealed monomolecular thin layer, a favored injection from the tip, though still visible, seems less pronounced compared with the nonannealed film, so that the curves are less asymmetric. We speculate that this could be due to an improved interface electronic structure after thermal annealing, which, in turn, results in improved charge injection from the gold electrode.

To investigate charge transport in the vertical direction, we performed local *I–V* measurements on different layers of the nanocrystals, the results are shown in **Figure 9**. The average current measured at fixed bias shows a clear decrease with increasing number of layers up to 6 ML structures (12 nm) (see also Figure S10, Supporting Information).

From the space charge limited current (SCLC) model, the charge carrier mobility μ can be extracted for devices built by sandwiching the organic layer between two electrodes. This regime corresponds to the current obtained when the number of injected charges reaches a maximum because their electrostatic potential prevents the injection of additional charges.[39]

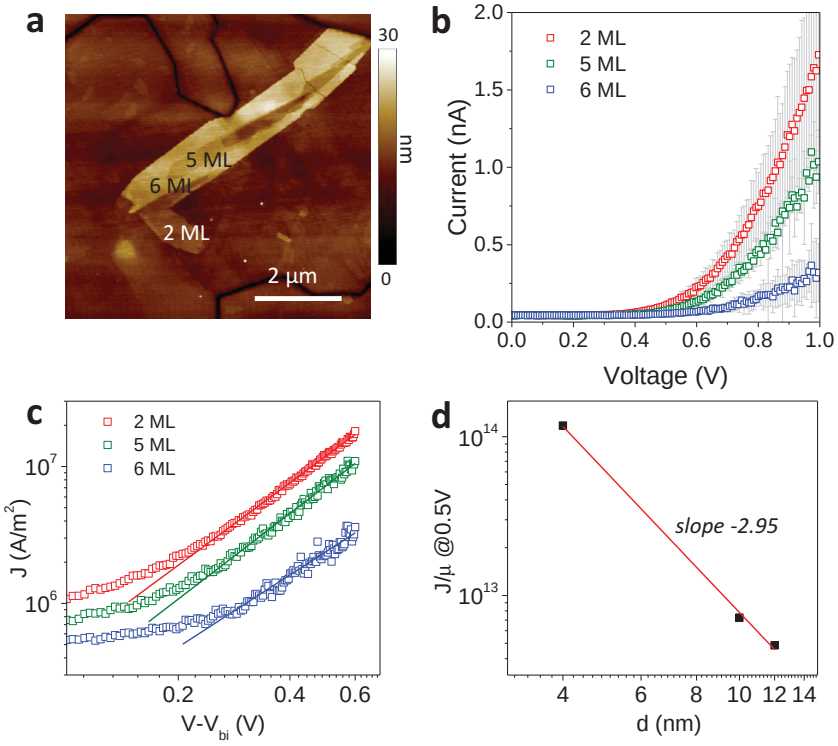

Figure 9. a) AFM image showing a layered structure where different layers are visible; b) current–voltage measurements performed on the layers marked as 2 ML, 5 ML, and 6 ML; c) fitting to SCLC model; d) plot showing the dependence on the thickness *d*.

C-AFM has been also employed to extract local mobility in organic materials in the framework of the SCLC regime.[40]

The current density J scales quadratically with the applied bias voltage V and is governed by the Mott–Gurney law:

$$J = \frac{9}{8}\varepsilon_0\varepsilon_r\mu\frac{V^2}{d^3}$$

where ε_0 is the permittivity in vacuum, ε_r is the dielectric constant of the material, V is the voltage drop across the device, and d is the distance between the electrodes. The experimental I–V curves are fitted to this law (Figure 9c,d), the details on the fitting are reported in Table S2 (Supporting Information).

The curves show a quadratic dependence on the voltage and, there from, the average charge mobility could be calculated to $(5.2 \pm 0.1)10^{-3}$ cm^2 V^{-1} s^{-1}. The dependence on the thickness was evaluated by plotting the current density versus the mobility as a function of the thickness, where a dependence of $J \propto d^{-3}$ was found. This seems to be in contradiction with recent work reported by Reid et al.[40a] that showed a deviation from the d^{-3} toward a d^{-1} dependence in SCLC measurements performed by C-AFM, which was caused by geometrical factors. Similar findings were discussed by Woellner et al.,[41] who modeled the current–voltage relation in the SCLC regime with geometrical effects, which were taken into account by introducing an enhancement factor $\lambda \leq 1$ defined as ratio of tip radius and sample thickness. However, the thickness of the present nanostructures is smaller than the AFM tip radius (20 nm),[28b] therefore, the present case approaches the Mott–Gurney law for planar electrodes.

3. Conclusion

In summary, we report a detailed study on the correlation between structural, morphological, and electrical properties of PDIF-CN_2 nanostructures obtained by the Langmuir–Blodgett technique and on the effect of their thermal annealing. A monomolecular-thin layer was obtained at the air/water interface and transferred onto different solid substrates. At high transfer pressures, the molecules adopted an upright standing conformation within the film, as evidenced by XRR and GIXRD. These films feature the photophysical characteristics of J-aggregates with pronounced absorption red-shift and negligible Stokes shift. The vertical charge transport probed by C-AFM junctions revealed higher resistance values compared with covalently linked, self-assembled monolayers and a clear rectification. The in-plane charge transport was probed both by C-AFM in horizontal configuration and in macroscopic field-effect transistors, showing an electron mobility as high as 3.1 $\times$ 10^{-2} cm^2 V^{-1} s^{-1}, which is comparable to those of the best performing p-type monolayer transistors available to date.

Postdeposition thermal annealing of the 2D LB monolayer induced a reorganization of the molecules on the surface forming 3D multilayered architectures, which exhibited morphological and photophysical properties comparable both to thermally annealed films formed by spin-coating and microscopic crystals obtained by solvent-induced precipitation. There, structural analysis revealed an upright standing molecular configuration similar to that of single crystals, maximizing the cofacial arrangement of the perylene cores. The out-of-plane charge transport properties of these nanostructures was probed by C-AFM and modelled in the framework of space-charge limited current yielding an average mobility for electrons of $(5.2 \pm 0.1)10^{-3}$ cm^2 V^{-1} s^{-1}.

The remarkable electrical characteristics of the present PDIF-CN_2 nanoarchitectures not only renders them ideal systems for fundamental studies on charge transport at the nanoscale, but also pave the way toward their exploitation in future downscaled organic electronic devices.

4. Experimental Section

Materials: N,N′-1H,1H-perfluorobutyl dicyanoperylenecarboxydiimide (PDIF-CN_2) (N1100 Polyera ActivInk) was solubilized in chloroform (Sigma-Aldrich, 99.9%) at a concentration of 1 mg mL^{-1}. For optical characterization in solution a concentration 1×10^{-5} M was used.

Films Fabrication: Langmuir–Blodgett experiments were carried out in a KSV minitrough apparatus by employing ultrapure MilliQ water with a resistivity of 18 MΩ cm as a subphase. Drops of the PDIF-CN_2 solution were randomly spread over the aqueous sub-phase. After few minutes to evaporate the solvent, the floating films were linearly compressed by the two mobile barriers at a rate of 5 mm min^{-1}. Surface-pressure versus molecular-area isotherms were recorded by film balance measurement (Wilhelmy plate method). The ultrathin film transfers were performed onto the different substrates by an upstroke operation at speed of 5 mm min^{-1}. The films were dried in vacuum oven at 30 °C and stored in nitrogen atmosphere before characterization. Spin-coated (SC) films having thickness of 5–10 nm were fabricated at speed of 1500 rpm for 60 s, from 150 µL of a solution 2 mg mL^{-1} in chloroform. Micrometric fibers were obtained by SIP method, by dropping 50 µL of solution 2 mg mL^{-1} in chloroform in 950 µL of methanol, as reported by Mativetsky et al.[26] For the postdeposition treatments, LB or SC samples were annealed on a hotplate in ambient atmosphere at 110 °C for 2 h.

Thin Film Transistors: Bottom-gate/bottom-contact small channels (channel lengths L = 2.5–20 µm) transistor devices were fabricated by transferring the films on SiO_2/Si^{n++} (silicon oxide on highly doped silicon) substrates with patterned interdigitated gold electrodes (Fraunhofer Institute for Photonic Microsystems IPMS, Dresden, Germany). Bottom gate/bottom contact long channels (channel lengths L = 60–120 µm) transistors were fabricated on SiO_2/Si^{n++} substrates (230 ± 10-nm thick SiO_2, Fraunhofer Institute for Photonic Microsystems IPMS, Dresden, Germany) on which 30-nm thick interdigitated gold electrodes were thermally evaporated through a shadow mask. All the substrates used for transistors fabrications were cleaned by subsequent ultrasonication bath in acetone and isopropanol prior to use. A Keithley 2636A source meter was employed for the OFETs characterization in the controlled atmosphere of a glovebox (O_2 and H_2O content below 10 and 2 ppm, respectively). XRR and GIXRD were performed at beamline ID10 at the European Synchrotron Radiation Facility (ESRF), Grenoble, France. Experimental parameters: primary beam energy: 22 keV, sample to detector distance: 355 mm, and beam size: 1 × 0.1 mm. For XRR, a LiF point detector with an evacuated secondary slit system was used. GIXRD was done by one-time exposure (60 s) using a PILATUS 300K (Dectris) 2D detector; all samples were measured under He flow to reduce sample degradation. GIXRD data transformation was done using the software xrayutilities,[42] analysis of the data using the software PyGID (TU-Graz, Austria); XRR data were fitted using the software Parratt32;[43] the scattering length densities for the layers in the XRR models at the given beam energy were calculated using online NIST software (http://www.ncnr.nist.gov/resources/activation/). The LB films for these characterizations were prepared on SiO_2/Si^{n++} substrates (Fraunhofer Institute for Photonic Microsystems IPMS, Dresden, Germany).

Photophysical Characterization: For optical measurements, absorption, and fluorescence spectra, the films were transferred on glass substrates, washed in acetone and isopropanol prior to use. Absorption spectra of films were recorded on a JASCO spectrophotometer – V670. For the fluorescence spectra, a spectrofluorimeter Fluorolog 3 by Jobin–Yvon in a front-face configuration was used to minimize the self-absorption (inner filter effect). Fluorescence microscopy images were taken on an Olympus BX51 microscope at λ_{ex} = 450–480 nm and λ_{em} > 515 nm. AFM and C-AFM Characterizations were carried out in a Multimode V (Veeco) microscope equipped with a Nanoscope V controller. For C-AFM junction fabrication the ultrathin films were transferred on epitaxial gold (111) substrates (Georg Albert PVD, Germany). Commercial silicon cantilevers with a nominal spring constant of 40 N m^{-1} were used for morphological characterization in tapping mode while Pt/Ir-coated silicon probes with a spring constant of 0.2 N m^{-1} were used to perform imaging in contact mode and local current–voltage measurements by applying a constant load force of 2×10^{-9} N. All the measurements were performed under nitrogen atmosphere, with a humidity level below 5%.

Supporting Information

Supporting Information is available from the Wiley Online Library or from the author.

Acknowledgements

This work was financially supported by the European Commission through ERC project SUPRAFUNCTION (Grant No. GA-257305) and the Marie-Curie ITN GENIUS (PITN-GA- 2010-264694), the Agence Nationale de la Recherche through the LabEx project Chemistry of Complex Systems (ANR-10-LABX-0026_CSC), and the International Center for Frontier Research in Chemistry (icFRC). We thank Katrein Sauer and Berthold Wegner for experimental support, Armin Moser (TU-Graz) for providing the software PyGID for GIXRD analysis, as well as Roland Resel (TU-Graz) and Dominik Kriegner (Charles University, Prague) for fruitful discussions on GIXRD. We acknowledge the ESRF for provision of synchrotron radiation facilities and we would like to thank Oleg Konovalov and Giovanni Li Destri for assistance in using beam line ID10.

Received: October 27, 2014
Revised: November 25, 2014
Published online: March 16, 2015

[1] a) E. C. P. Smits, S. G. J. Mathijssen, P. A. van Hal, S. Setayesh, T. C. T. Geuns, K. A. H. A. Mutsaers, E. Cantatore, H. J. Wondergem, O. Werzer, R. Resel, M. Kemerink, S. Kirchmeyer, A. M. Muzafarov, S. A. Ponomarenko, B. de Boer, P. W. M. Blom, D. M. de Leeuw, *Nature* **2008**, *455*, 956; b) L. Li, P. Gao, K. C. Schuermann, S. Ostendorp, W. Wang, C. Du, Y. Lei, H. Fuchs, L. D. Cola, K. Müllen, L. Chi, *J. Am. Chem. Soc.* **2010**, *132*, 8807; c) S. Fabiano, C. Musumeci, Z. Chen, A. Scandurra, H. Wang, Y.-L. Loo, A. Facchetti, B. Pignataro, *Adv. Mater.* **2012**, *24*, 951; d)S. Wang, A. Kiersnowski, W. Pisula, K. Müllen, *J. Am. Chem. Soc.* **2012**, *134*, 4015; e) S. G. J. Mathijssen, E. C. P. Smits, P. A. v. Hal, H. J. Wondergem, S. A. Ponomarenko, A. Moser, R. Resel, P. A. Bobbert, M. Kemerink, R. A. J. Janssen, D. M. d. Leeuw, *Nat. Nanotech.* **2009**, *4*, 674.

[2] A. Facchetti, M.-H. Yoon, T. J. Marks, *Adv. Mater.* **2005**, *17*, 1705.

[3] a) G. S. Tulevski, Q. Miao, M. Fukuto, R. Abram, B. Ocko, R. Pindak, M. L. Steigerwald, C. R. Kagan, C. Nuckolls, *J. Am. Chem. Soc.* **2004**, *126*, 15048; b) Y. Cao, M. L. Steigerwald, C. Nuckolls, X. Guo, *Adv. Mater.* **2010**, *22*, 20; c) C. M. Jäger, T. Schmaltz, M. Novak, A. Khassanov, A. Vorobiev, M. Hennemann, A. Krause, H. Dietrich, D. Zahn, A. Hirsch, M. Halik, T. Clark, *J. Am. Chem. Soc.* **2013**, *135*, 4893; d) M. Novak, A. Ebel, T. Meyer-Friedrichsen, A. Jedaa, B. F. Vieweg, G. Yang, K. Voitchovsky, F. Stellacci, E. Spiecker, A. Hirsch, M. Halik, *Nano Lett.* **2011**, *11*, 156; e) A. Rumpel, M. Novak, J. Walter, B. Braunschweig, M. Halik, W. Peukert, *Langmuir* **2011**, *27*, 15016.

[4] K. Asadi, Y. Wu, F. Gholamrezaie, P. Rudolf, P. W. M. Blom, *Adv. Mater.* **2009**, *21*, 4109.

[5] B. A. Jones, A. Facchetti, M. R. Wasielewski, T. J. Marks, *J. Am. Chem. Soc.* **2007**, *129*, 15259.

[6] C. Li, H. Wonneberger, *Adv. Mater.* **2012**, *24*, 613.

[7] X. Zhan, A. Facchetti, S. Barlow, T. J. Marks, M. A. Ratner, M. R. Wasielewski, S. R. Marder, *Adv. Mater.* **2011**, *23*, 268.

[8] B. A. Jones, M. J. Ahrens, M. H. Yoon, A. Facchetti, T. J. Marks, M. R. Wasielewski, *Angew. Chem. Int. Ed. Engl.* **2004**, *43*, 6363.

[9] a) A. S. Molinari, H. Alves, Z. Chen, A. Facchetti, A. F. Morpurgo, *J. Am. Chem. Soc.* **2009**, *131*, 2462; b) S. Ono, N. Minder, Z. Chen, A. Facchetti, A. F. Morpurgo, *Appl. Phys. Lett.* **2010**, *97*, 143307; c) K. Willa, R. Häusermann, T. Mathis, A. Facchetti, Z. Chen, B. Batlogg, *J. Appl. Phys.* **2013**, *113*, 133707.

[10] J. Soeda, T. Uemura, Y. Mizuno, A. Nakao, Y. Nakazawa, A. Facchetti, J. Takeya, *Adv. Mater.* **2011**, *23*, 3681.

[11] a) Y. G. Ha, J. D. Emery, M. J. Bedzyk, H. Usta, A. Facchetti, T. J. Marks, *J. Am. Chem. Soc.* **2011**, *133*, 10239; b) F. Chiarella, M. Barra, L. Ricciotti, A. Aloisio, A. Cassinese, *Electronics* **2014**, *3*, 76.

[12] C. Piliego, D. Jarzab, G. Gigli, Z. Chen, A. Facchetti, M. A. Loi, *Adv. Mater.* **2009**, *21*, 1573.

[13] S. Fabiano, H. Wang, C. Piliego, C. Jaye, D. A. Fischer, Z. Chen, B. Pignataro, A. Facchetti, Y.-L. Loo, M. A. Loi, *Adv. Funct. Mater.* **2011**, *21*, 4479.

[14] G. Xu, Z. Bao, J. T. Groves, *Langmuir* **2000**, *16*, 1834.

[15] A. S. Sizov, E. V. Agina, F. Gholamrezaie, V. V. Bruevich, O. V. Borshchev, D. Y. Paraschuk, D. M. de Leeuw, S. A. Ponomarenko, *Appl. Phys. Lett.* **2013**, *103*, 043310.

[16] Y. Cao, Z. Wei, S. Liu, L. Gan, X. Guo, W. Xu, M. L. Steigerwald, Z. Liu, D. Zhu, *Angew. Chem. Int. Ed.* **2010**, *49*, 6319.

[17] S. Fabiano, H. Yoshida, Z. Chen, A. Facchetti, M. A. Loi, *ACS Appl. Mater. Interfaces* **2013**, *5*, 4417.

[18] V. M. Kaganer, H. Möhwald, P. Dutta, *Rev. Mod. Phys.* **1999**, *71*, 779.

[19] S. S. Batsanov, *Inorg. Mater.* **2001**, *37*, 1031.

[20] G. J. Ashwell, *Thin Solid Films* **1990**, *186*, 155.

[21] L. G. Parratt, *Phys. Rev.* **1954**, *95*, 359.

[22] A. Ringk, W. S. Christian Roelofs, E. C. P. Smits, C. van der Marel, I. Salzmann, A. Neuhold, G. H. Gelinck, R. Resel, D. M. de Leeuw, P. Strohriegl, *Org. Electron.* **2013**, *14*, 1297.

[23] S. C. B. Mannsfeld, A. Virkar, C. Reese, M. F. Toney, Z. N. Bao, *Adv. Mater.* **2009**, *21*, 2294.

[24] a) R. T. Weitz, K. Amsharov, U. Zschieschang, E. B. Villas, D. K. Goswami, M. Burghard, H. Dosch, M. Jansen, K. Kern, H. Klauk, *J. Am. Chem. Soc.* **2008**, *130*, 4637; b) R. Rödel, F. Letzkus, T. Zaki, J. N. Burghartz, U. Kraft, U. Zschieschang, K. Kern, H. Klauk, *Appl. Phys. Lett.* **2013**, *102*, 233303.

[25] C. Piliego, F. Cordella, D. Jarzab, S. Lu, Z. Chen, A. Facchetti, M. A. Loi, *Appl. Phys. A* **2008**, *95*, 303.

[26] J. M. Mativetsky, E. Orgiu, I. Lieberwirth, W. Pisula, P. Samorì, *Adv. Mater.* **2014**, *26*, 430.

[27] B. A. Jones, A. Facchetti, M. R. Wasielewski, T. J. Marks, *Adv. Funct. Mater.* **2008**, *18*, 1329.

[28] a) S. H. Choi, C. D. Frisbie, *J. Am. Chem. Soc.* **2010**, *132*, 16191; b) J. M. Mativetsky, G. Pace, M. Elbing, M. A. Rampi, M. Mayor, P. Samorì, *J. Am. Chem. Soc.* **2008**, *130*, 9192.

[29] a) P. E. Kornilovitch, A. M. Bratkovsky, R. Stanley Williams, *Phys. Rev. B* **2002**, *66*, 165436; b) C. Krzeminski, C. Delerue, G. Allan, D. Vuillaume, R. Metzger, *Phys. Rev. B* **2001**, *64*, 085405.
[30] M. C. R. Delgado, E.-G. Kim, D. t. A. d. S. Filho, J.-L. Brédas, *J. Am. Chem. Soc.* **2010**, *132*, 3375.
[31] N. Gaillard, M. Gros-Jean, D. Mariolle, F. o. Bertin, A. Bsiesy, *Appl. Phys. Lett.* **2006**, *89*, 154101.
[32] K. Emmanouil, P. Gawrys, M. Zagorska, S. Kennou, *Microelectron. Eng.* **2013**, *112*, 170.
[33] B. L. Hendriksen, F. Martin, Y. Qi, C. Mauldin, N. Vukmirovic, J. Ren, H. Wormeester, A. J. Katan, V. Altoe, S. Aloni, J. M. Fréchet, L. W. Wang, M. Salmeron, *Nano Lett.* **2011**, *11*, 4107.
[34] R. Agrawal, S. Ghosh, *Appl. Phys. Lett.* **2006**, *89*, 222114.
[35] a) T. W. Kelley, C. D. Frisbie, *J. Vac. Sci. Technol. B* **2000**, *18*, 632; b) M. Kemerink, S. Alvarado, P. Müller, P. Koenraad, H. Salemink, J. Wolter, R. Janssen, *Phys. Rev. B* **2004**, *70*, 045202.
[36] D. Natali, M. Caironi, *Adv. Mater.* **2012**, *24*, 1357.
[37] A. Ringk, X. Li, F. Gholamrezaie, E. C. P. Smits, A. Neuhold, A. Moser, C. Van der Marel, G. H. Gelinck, R. Resel, D. M. de Leeuw, P. Strohriegl, *Adv. Funct. Mater.* **2013**, *23*, 2016.
[38] a) T. Schmaltz, A. Y. Amin, A. Khassanov, T. Meyer-Friedrichsen, H. G. Steinruck, A. Magerl, J. J. Segura, K. Voitchovsky, F. Stellacci, M. Halik, *Adv. Mater.* **2013**, *25*, 4511; b) F. Gholamrezaie, S. G. Mathijssen, E. C. Smits, T. C. Geuns, P. A. van Hal, S. A. Ponomarenko, H. G. Flesch, R. Resel, E. Cantatore, P. W. Blom, D. M. de Leeuw, *Nano Lett.* **2010**, *10*, 1998; c) M. Defaux, F. Gholamrezaie, J. Wang, A. Kreyes, U. Ziener, D. V. Anokhin, D. A. Ivanov, A. Moser, A. Neuhold, I. Salzmann, R. Resel, D. M. de Leeuw, S. C. J. Meskers, M. Moeller, A. Mourran, *Adv. Mater.* **2012**, *24*, 973; d) E. M. Mannebach, J. W. Spalenka, P. S. Johnson, Z. Cai, F. J. Himpsel, P. G. Evans, *Adv. Funct. Mater.* **2013**, *23*, 554.
[39] a) P. W. M. Blom, M. J. M. de Jong, J. J. M. Vleggaar, *Appl. Phys. Lett.* **1996**, *68*, 3308; b) V. Coropceanu, J. Cornil, D. A. d. S. Filho, Y. Olivier, R. Silbey, J.-L. Brédas, *Chem. Rev.* **2007**, *107*, 926.
[40] a) O. G. Reid, K. Munechika, D. S. Ginger, *Nano Lett.* **2008**, *8*, 1602; b) R. Yang, A. Garcia, D. Korystov, A. Mikhailovsky, G. C. Bazan, T.-Q. Nguyen, *J. Am. Chem. Soc.* **2006**, *128*, 16532; c) H.-N. Lin, H.-L. Lin, S.-S. Wang, L.-S. Yu, G.-Y. Perng, S.-A. Chen, S.-H. Chen, *Appl. Phys. Lett.* **2002**, *81*, 2572; d) C. Ionescu-Zanetti, A. Mechler, S. A. Carter, R. Lal, *Adv. Mater.* **2004**, *16*, 385; e) O. Douhéret, L. Lutsen, A. Swinnen, M. Breselge, K. Vandewal, L. Goris, J. Manca, *Appl. Phys. Lett.* **2006**, *89*, 032107.
[41] C. F. Woellner, J. A. Freire, M. Guide, T. Q. Nguyen, *J. Chem. Phys.* **2011**, *135*, 084108.
[42] D. Kriegner, E. Wintersberger, J. Stangl, *J. Appl. Cryst.* **2013**, *46*, 1162.
[43] C. Braun, HMI Berlin, Germany **2002**.